

BIOCHEMISTRY

Structures and membrane interactions of human OAT1 in complex with clinical used drugs

Xuening Wu^{1†}, Yongbo Luo^{2†}, Shijian Feng^{1†}, Haiyun Ma^{2†}, Bowen Ke^{3*}, Kunjie Wang^{1*}, Zhaoming Su^{2*}, Dongxue Yang^{1*}

Organic anion transporters (OATs) in mammals mediate the renal excretion of numerous structurally diverse organic anionic compounds. Therapeutically inhibiting OATs has emerged as a strategy to modulate the elimination or retention of these substrates. Among them, OAT1 plays a pivotal role in the pharmacokinetics and drug-drug interactions of a wide range of prescription medications. Despite extensive structural investigations, the molecular structure, and basis of polyspecific anionic drug recognition of human OAT1 (hOAT1) have remained elusive. Here, we present cryogenic electron microscopy structures of hOAT1 and its complexes with the antiviral drug cidofovir and an FDA-approved type II diabetes medication glibenclamide, respectively. Our findings reveal that both cidofovir and glibenclamide bind to a central binding site, capturing the transporter in inward-facing conformations. These structures elucidate how specific residues within the central site orchestrate the binding of chemically diverse inhibitors and provide a structural basis for the drug recognition mechanism of hOAT1.

Copyright © 2025 The Authors, some rights reserved; exclusive licensee American Association for the Advancement of Science. No claim to original U.S. Government Works. Distributed under a Creative Commons Attribution NonCommercial License 4.0 (CC BY-NC).

INTRODUCTION

Organic anion transporters (OATs), part of the solute carrier 22 (SLC22) superfamily, are integral membrane proteins that facilitate the transport of a broad range of substrates, including organic anions, zwitterions, and cations. These transporters are expressed in various tissues such as the kidney, brain, liver, intestine, and placenta, where they play crucial roles in the physiological elimination of endogenous and xenobiotic substances (1–5). The SLC22 family is composed of OATs, organic cation transporters (OCTs), and more specialized transporters such as URAT1 (also known as SLC22A12) (6). OATs exhibit promiscuous substrate specificity ranging from organic anions to organic zwitterions and organic cations, as well as other molecules (7–9). Mutations in OATs can be linked to metabolic diseases and hereditary disorders, causing dysfunction in the elimination of toxic metabolites or the uptake of essential nutrients, contributing to various pathologies (10–15).

Among this superfamily, OAT1 (SLC22A6) is predominantly localized in the basolateral membrane of kidney proximal tubule cells, serving vital roles in metabolite uptake and the transport of clinically relevant drugs such as anti-HIV drugs, antitumor agents, antibiotics, and other pharmaceuticals (16–20). Furthermore, OAT1 facilitates the transport of harmful compounds, including chratoxin A (21), aristolochic acid (21), organo-Hg complexes (22), and indoxyl sulfate (23). Dysfunction of OAT1 is particularly detrimental; it can compromise the elimination of xenobiotics and has implications for conditions like chronic kidney disease (24). The transport mechanism of OAT1 involves the exchange of organic anions for intracellular dicarboxylates, like α -ketoglutarate, whose intracellular

concentrations are maintained by metabolic processes and sodium-coupled transporters (25–27). OAT1's functional status is crucial for both renal pathophysiology and pharmacokinetics, as it influences the efficiency of drug clearance and therapeutic efficacy.

OAT1 plays crucial roles in physiological elimination, renal pathophysiology, and pharmacokinetics. For instance, OAT1 exhibits high affinity ($K_i = 0.6 \mu\text{M}$) for aristolochic acids, which has been linked to Balkan nephropathy (28). In addition, various drug-induced nephrotoxicities mediated by OAT have been documented in several studies (10). Pharmacologically, the bioavailability of numerous drugs relies on the OAT. Cidofovir are nucleoside phosphonate analogs, a class of novel antivirals structurally related to natural nucleotides, has been approved for the treatment of cytomegalovirus retinitis in patients with AIDS (29). Cidofovir is actively secreted by the kidney, presumably via hOAT1, and the main dose-limiting toxicity is nephrotoxicity (30, 31). To reduce this adverse event, cidofovir is used in conjunction with probenecid, an inhibitor of organic anion transport (29). Glibenclamide, which belongs to sulfonylureas, is administered to patients with type 2 diabetes (32). The pharmacological effect of glibenclamide is demonstrated through the induction of insulin secretion, achieved by blocking adenosine 5'-triphosphate-sensitive K^+ channels in pancreatic β cells (33). In clinical scenarios, there are numerous combination medications that can lead to hypoglycemia as a side effect, primarily by elevating the plasma concentration of sulfonylureas (34). Probenecid is among these medications. The proposed mechanism for this interaction suggests that probenecid may suppress the renal secretion of sulfonylureas via the organic anion transport system.

Because of the crucial role of OAT1 in renal clearance, it exerts a notable influence on drug pharmacokinetics, in particular in absorption distribution, metabolism, and elimination (ADME). Therefore, it is essential to establish the impact of transport proteins on ADME and potential drug-drug interactions (DDIs) that may arise from the concurrent use of multiple drugs for therapeutic purposes across different indications.

Extensive structural and functional studies on OCT1 (35, 36) and OCT3 (37), together with recent investigations of rat OAT1 (35, 38), have shown how an inverted pseudo-repeat of six transmembrane

¹Department of Urology, Institute of Urology (Laboratory of Reconstructive Urology), West China Hospital, Sichuan University, Chengdu, Sichuan 610044, China.

²The State Key Laboratory of Biotherapy, Department of Geriatrics and National Clinical Research Center for Geriatrics, West China Hospital, Sichuan University, Chengdu, Sichuan 610044, China. ³Department of Anesthesiology, Laboratory of Anesthesia and Critical Care Medicine, West China Hospital, Sichuan University, Chengdu, Sichuan 610041, China.

*Corresponding author. Email: yangdx@scu.edu.cn (D.Y.); zsu@wchscu.cn (Z.S.); wzwzlwww@qq.com (K.W.); bowenke@scu.edu.cn (B.K.)

†These authors contributed equally to this work.

(TM) helices creates the conserved fold of the major facilitator superfamily (MFS). A ligand-binding site is approximately halfway across the membrane. These binding sites become alternately accessible to the extracellular and intracellular spaces as transporters transition between different states in their transport cycles.

The structural and functional versatility of OAT1 poses risks for DDIs, in particular when multiple drugs vie for the same transport pathway (39–42). This competition can alter therapeutic outcomes and exacerbate toxicity. Understanding OAT1's role in renal clearance has led to the exploration of OAT1 inhibitors as a strategy to elevate therapeutic drug levels while mitigating adverse effects, with co-administration of probenecid in certain treatments serving as an example (43, 44). The development of specific OAT1 inhibitors would enable more targeted intervention and clinical options to enhance the effectiveness of chemotherapeutics and other medications.

Although rat OAT1 (rOAT1) is frequently used in drug development due to its high sequence identity (88%) and similarity (97%) to human OAT1 (hOAT1) (fig. S1), substantial discrepancies exist in the interaction profiles with various drugs. For instance, the affinity for methotrexate, critical in cancer treatments, differs drastically between species. hOAT1 facilitates the transport of the cytostatic methotrexate with a very low affinity (K_m , 724 μM) in *Xenopus laevis* oocytes, while the rOAT1-mediated methotrexate transport in transfected LLC-PK1 cells revealed a high affinity with a K_m value of 0.87 to 14.9 μM (22, 45), indicating caution should be exercised in translating rodent data to human pharmacokinetics.

Besides, the precise mechanisms that underlie hOAT1's substrate discrimination remain largely unknown, posing a challenge for specific inhibitor design targeting hOAT1. To address these gaps, our study used mild nonionic detergents to purify hOAT1 and employed size exclusion chromatography (SEC) for analysis. High-resolution single-particle cryo-electron microscopy (cryo-EM) was subsequently used to elucidate the structural features of hOAT1 and its complexes with clinically relevant drugs cidofovir and glibenclamide. Together with mutagenesis functional studies and molecular dynamics (MD) simulations, our findings offer valuable insights into the mechanisms of ligand recognition and provide structural basis for the development of specific inhibitors that can optimize therapeutic regimens.

RESULTS

Purification and characterization of hOAT1

To investigate the oligomerization state of hOAT1, we examined the mild nonionic detergents, aiming to extract the transporter under the mildest conditions. We examined *n*-dodecyl- β -D-maltoside (DDM) together with cholesterol hemisuccinate (CHS), Lauryl maltose neopentyl glycol, and glyco-diosgenin, respectively (fig. S2A). hOAT1 exhibited similar profiles of fluorescence SEC and DDM was applied in the following study.

We also compared the elution position of hOAT1 with the monomeric rOAT1, and the coelution of the two peaks supported the conclusion that hOAT1, solubilized in the presence of DDM/CHS, behaved as a monomeric entity (fig. S2B). The well-resolved and symmetrical SEC peak indicated that the purified hOAT1 was monodisperse and best described as a single species.

To explore the function of hOAT1, we then carried out cell-based transport experiment using 6-carboxyfluorescein (6-CF), a common fluorescent substrate of OAT1, in human embryonic kidney (HEK) 293/hOAT1 cells. We confirmed the specific uptake of 6-CF

by hOAT1, and K_m for saturation was 13.7 μM (fig. S2C and Fig. 1A), which is consistent with the literature (46). To investigate the discrimination between different compounds of hOAT1, we used two different sizes of drugs, cidofovir and glibenclamide. Cidofovir, an antiviral agent approved by the US Food and Drug Administration (FDA) for the treatment of CMV retinitis in patients with AIDS (47), is a high-affinity substrate for hOAT1 (48). Glibenclamide (also known as glyburide in the United States) is an FDA-approved drug commonly used in patients with type 2 diabetes (32) and is also a known inhibitor of OAT (22). To verify the potency of the interaction between the two drugs and hOAT1, we evaluated the inhibitory effect of cidofovir and glibenclamide on the uptake of 6-CF in a dose-dependent manner. The 6-CF uptake was *cis*-inhibited by increasing concentrations of cidofovir and glibenclamide. The half-maximal inhibitory concentration (IC_{50}) was $140.8 \pm 32.6 \mu\text{M}$ and $2.4 \pm 0.8 \mu\text{M}$, respectively (Fig. 1, B to D). These results suggested that both cidofovir and glibenclamide strongly interacted with hOAT1.

Structural determination of apo hOAT1

We then carried out a single-particle cryo-EM reconstruction of the apo hOAT1 (fig. S2, D and E) and obtained a density map at 3.36 Å resolution. Particle picking was employed with an elliptical “blob” of sufficient size to capture hOAT1 oligomers. Thorough two-dimensional (2D) and 3D classifications yielded only a single class of hOAT1 shown as a monomeric entity, with no evidence of trimers or higher-ordered oligomers (fig. S3 and table S1). This was consistent with the molecular size of hOAT1 estimated by SEC (fig. S2, D and E). The well-resolved density map allowed assignment of most amino acid side chains (fig. S4A). Akin to rOAT1, hOAT1 has three major domains regarding to their locations: TM domain (TMD), intracellular domain (ICD), and extracellular domain (ECD). The TMD comprises 12 TM helices that adopt the conserved fold of the MFS, with TMs 1–6 and 7–12 related by a pseudo-twofold axis. The ICD consists of seven helices with a four-helix bundle packs against the C-terminal end of TM6. The ECD consists of four *N*-linked glycosylation sites, and this domain has been indicated to involved in protein trafficking and dimerization (49, 50), but its exact function remains further elucidated. The structure can also be divided into two major domains based on their boundaries: N-terminal domain (NTD) and C-terminal domain (CTD). We have also observed a nonprotein density at the central binding site (fig. S4A). Given that hOAT1 is capable of facilitating the renal uptake of a wide range of endogenous and exogenous compounds, and considering that the apo hOAT1 was isolated in the absence of ligands, it is likely that this density represents an endogenous ligand. However, because of the resolution limit, it is currently not possible to identify the specific ligand from the shape of the density. Comparison of apo-hOAT1 with known structures of rOAT1 and other transporters enabled unambiguous assignment as the inward-open conformation (Fig. 2 and fig. S5).

Structural basis for cidofovir and glibenclamide recognition

To further understand the molecular basis for drug interaction, we determined the structure of hOAT1 in complex with cidofovir and glibenclamide at 3.15 and 3.68 Å, respectively (figs. S6 to S8 and table S1). The electron density maps are well resolved to enable accurate model building. Cidofovir-bound hOAT1 adopted an inward-facing conformation with the substrate pocket fully exposed to the cytoplasm but closed to the extracellular side (Fig. 3, A to C).

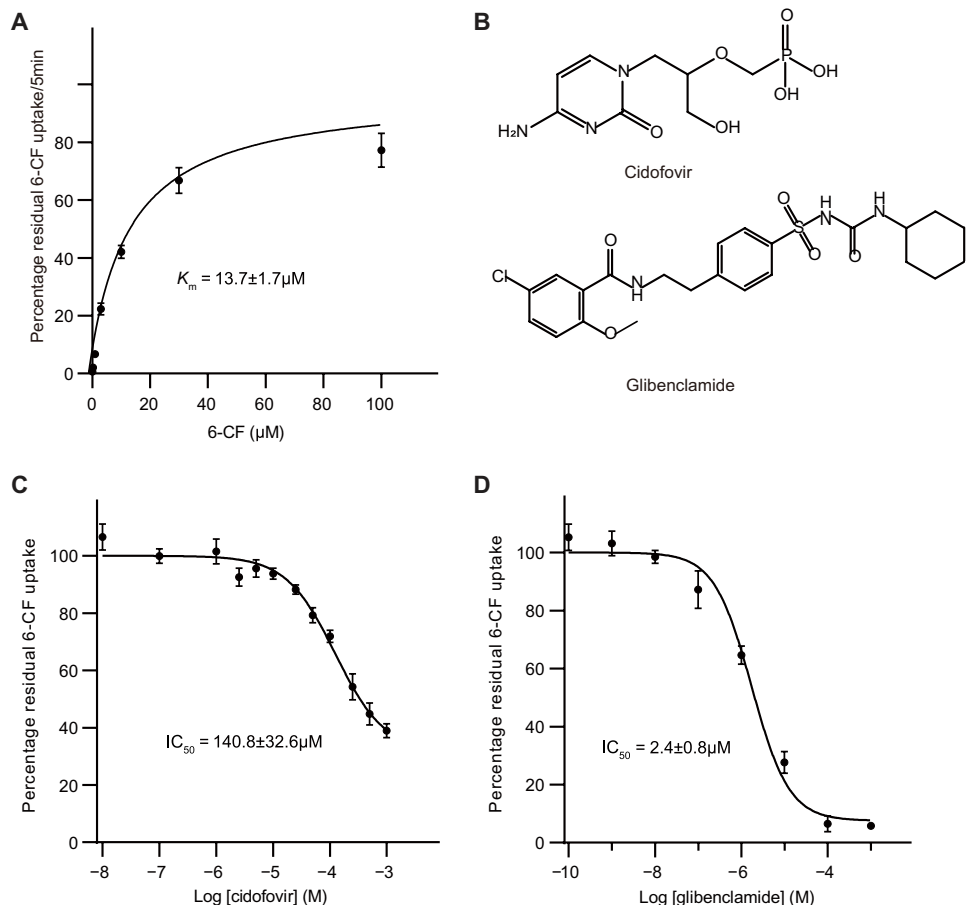


Fig. 1. Functional characterization of hOAT1. (A) Cell-based transport assay for wild-type (WT) hOAT1 with 6-CF, K_m for WT is $13.7 \pm 1.7 \mu\text{M}$, data are means \pm SEM. (B) Chemical structures of cidofovir and glibenclamide. (C) Plots of competition binding of cidofovir against 6-CF. Data are means \pm SEM. (D) Competition binding of glibenclamide against 6-CF. Error bars show the SEM.

The cidofovir ligand density was clearly identified in a confined pocket in the cryo-EM map (Fig. 3C). The ligand model was docked into the EM density and validated by MD simulations (Fig. 3D and fig. S9, A and B). Notably, cidofovir has a “loose” fit to the central site, neither spanning the entire binding pocket nor fully occupying the volume of the central site. We observed that the cidofovir adopts an extended configuration with the nucleoside group making an aromatic π - π interaction with Tyr²³⁰ (TM5) and Phe⁴³⁸ (TM10). The hydroxyl group of Tyr³⁵³ (TM7) forms a hydrogen bond with the carbonyl group of cidofovir. The amino group interacts with Ser²³¹ (TM5) and N439 (TM10) (Fig. 3, C and D). We then conducted a comprehensive analysis of the binding site to validate the observed interactions. An alanine mutant of Ser²³¹ and a tyrosine mutant of Phe⁴³⁸ resulted in the reduction of transport activity. However, the IC_{50} value for cidofovir inhibition increased from $140.8 \pm 32.6 \mu\text{M}$ for wild type to $344.3 \pm 152.4 \mu\text{M}$ for Ser²³¹ Ala and $1.401 \pm 0.66 \text{ mM}$ for Phe⁴³⁸ Tyr, further confirming their involvement in cidofovir interactions (Fig. 3, E and F).

Cidofovir is a nucleotide analog of cytosine that belongs to the class of acyclic nucleoside phosphonates and is the representative of this class recommended for the treatment of human cytomegalovirus retinitis, especially in HIV-infected patients (29). Tendofovir is an acyclic nucleoside analog of adenosine that also demonstrates

activity against hepatitis B virus and HIV (44). Previous structural study indicated that tendofovir has similar chemical structure to cidofovir but forms U shape to accommodate the binding site of rOAT1 (35). We compared the binding sites of cidofovir and tendofovir and observed both of the nucleoside groups forms aromatic interaction with Phe⁴³⁸ (TM10). The amino groups adopt different orientations, as the amino group of tendofovir interacts with Tyr³⁵⁴, closely associates with Ser³⁵⁰ and forms an anion- π interaction, while the amino group of cidofovir extends between TM5 and TM10 to interact with Ser²³¹ and Asn⁴³⁹ (fig. S9, A and B). Overall, the two drugs form similar interaction networks with OAT1, consistent with the functional assay results that showed similar IC_{50} s (IC_{50} for cidofovir was $140.8 \pm 32.6 \mu\text{M}$, for tendofovir was $120 \pm 19 \mu\text{M}$). However, both of the drugs do not fully occupy the binding pocket, leaving the site formed by TM1, TM2, TM4, and TM11 vacant. The spacious nature of the central site likely underlies the substrate promiscuity of the transporter.

Another drug glibenclamide also captured hOAT1 in an inward-facing conformation (fig. S10, C and D). The glibenclamide-bound hOAT1 structure allowed unambiguously docking of the ligand in the central site, which was further validated by MD simulations (Fig. 4A and fig. S9, C and D). Glibenclamide adopts a U shape at the apex of the central cavity of hOAT1 and binds within a pocket

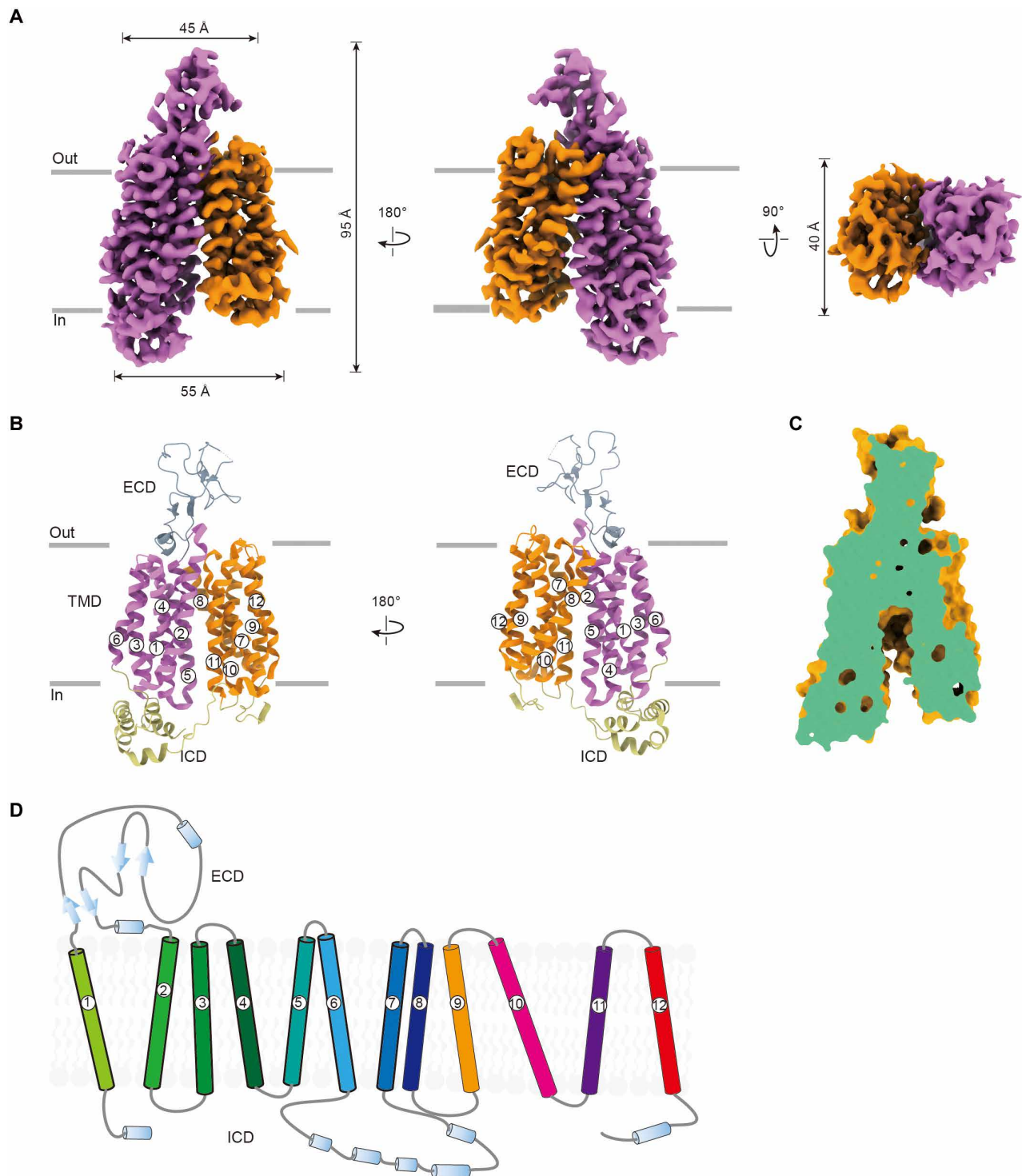


Fig. 2. Architecture of apo-hOAT1 in its inward-facing conformation. (A) Cryo-EM density map of hOAT1 in the inward-facing conformation. The NTD and CTD of hOAT1 are colored purple and orange, respectively. (B) Atomic model of hOAT1 with the NTD and CTD colored purple and orange, and the ECD and ICD colored gray and yellow green, respectively. (C) Slab view of the extracellular and intracellular cavities of hOAT1. (D) Schematic diagram of the secondary structures of hOAT1.

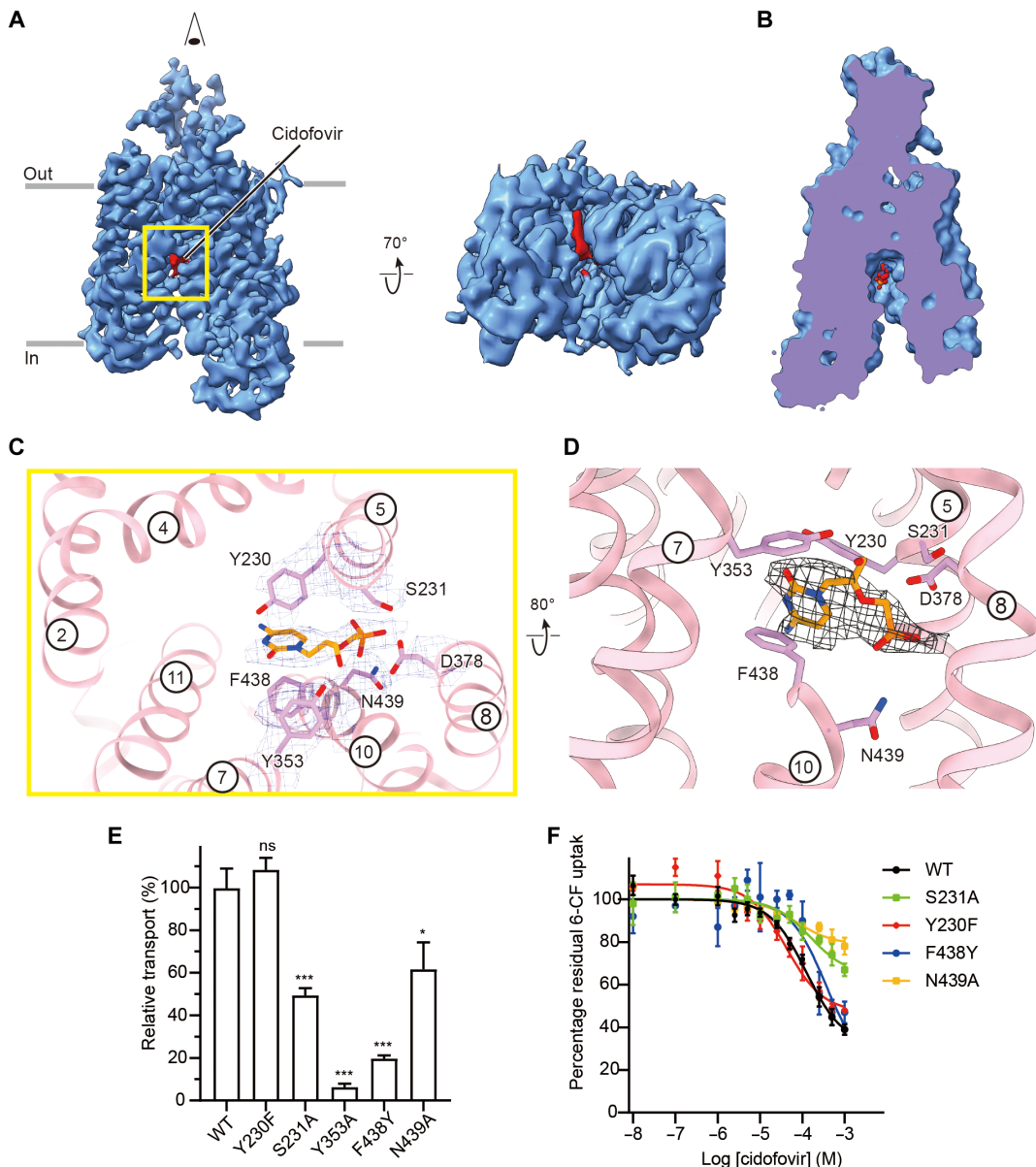


Fig. 3. Cryo-EM structure of hOAT1 in complex with cidofovir. (A) Cryo-EM density map of cidofovir in complex with hOAT1. The cidofovir was colored red. (B) Slab view of the extracellular and intracellular cavities of the cidofovir-hOAT1 complex. (C) Cidofovir interactions within the central binding site. (D) Different view for substrate binding sites. (E) Cell-based transport assays for WT and mutant hOAT1. Symbols show the mean values derived from $n = 3$ technical replicates. Error bars show the SEM, ns, $P > 0.05$; * $P \leq 0.05$; ** $P \leq 0.01$; and *** $P \leq 0.001$. (F) Competition binding of cidofovir against 6-CF with WT ($IC_{50}: 140.8 \pm 32.6 \mu\text{M}$) and S231A ($IC_{50}: 344.3 \pm 152.4 \mu\text{M}$), Y230F ($IC_{50}: 57.57 \pm 20.36 \mu\text{M}$), F438Y ($IC_{50}: 1.401 \pm 0.66 \text{ mM}$), and N439A ($IC_{50}: 225.14 \pm 212.96 \mu\text{M}$) mutants. Data are means \pm SEM.

formed by TM1, TM4, TM5, TM7, TM10, and TM11. Glibenclamide is a second-generation sulfonylurea containing a sulfonylurea group and a benzamido moiety (32). Key features include extension of the benzamide group toward TM10 and TM11 and interaction of the sulfonylurea group with TM1 and TM5. The cyclohexyl moiety protrudes into a cavity between TM1 and TM11. The binding site of glibenclamide is formed by hOAT1 residues Asn³⁵, Ser²⁰³, Met²⁰⁷, Tyr²³⁰, Tyr³⁵³, Tyr³⁵⁴, Phe⁴³⁸, Phe⁴⁴², Ser⁴⁶², and Arg⁴⁶⁶. Asn³⁵ from TM1, Tyr²³⁰ from TM5, and Tyr³⁵⁴ from TM7 form hydrogen bonds with the sulfonylurea group and Phe⁴⁴² from TM10 engages in aromatic interactions with the sulfonylurea group (Fig. 4B). We then

performed a detailed analysis of the binding site to confirm the interactions of these residues with glibenclamide. We mutated them individually and analyzed the resulting uptake activity and glibenclamide binding affinity. The Ser⁴⁶² Ala and Arg⁴⁶⁶ Ala only preserved less than 10% of the transport activity. The Met³¹ Ala, Tyr³⁵⁴ Ala, and Phe⁴⁴² Ala retained sufficient function to analyze their binding with glibenclamide, showing a reduction in the glibenclamide binding affinity in comparison with that of wild-type hOAT1 ($2.4 \pm 0.8 \mu\text{M}$; M31A, $11.4 \pm 5.4 \mu\text{M}$; Y354A, $7.5 \pm 3.2 \mu\text{M}$; and F442A, $17.7 \pm 12 \mu\text{M}$). Tyr²³⁰Phe has previously been implicated in substrate specificity for OAT1 (51), and in our assays, the

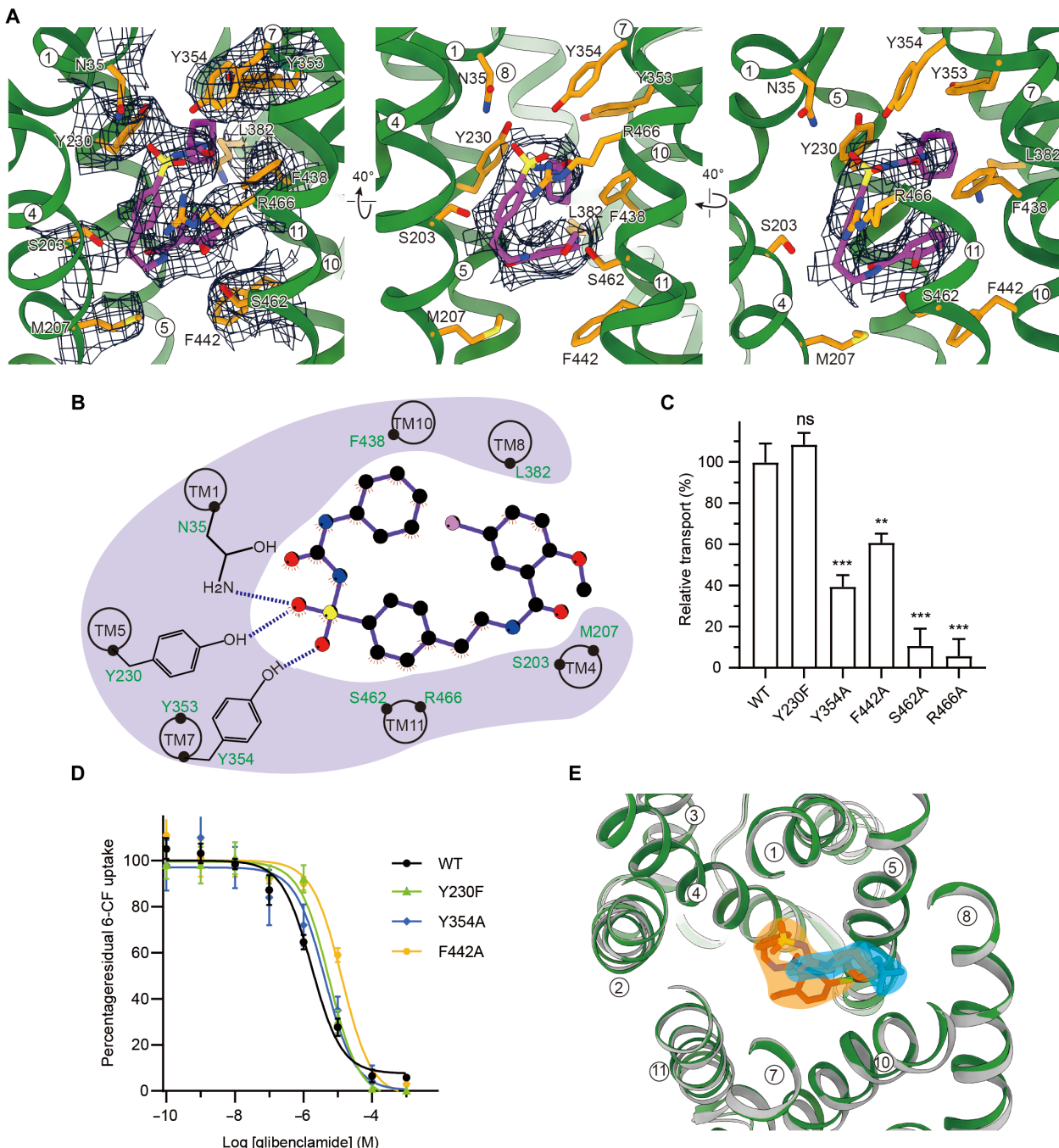


Fig. 4. Recognition of glibenclamide. (A) Zoomed-in view of the glibenclamide (purple) binding site. Glibenclamide is shown fitting into a density feature at the binding site with the involved hOAT1 backbone structures (green) annotated. Parts of hOAT1 have been removed for clarity. (B) Interactions between glibenclamide and hOAT1. Schematics are generated by LIGPLOT+. Each eyelash motif indicates a hydrophobic contact. (C) Cell-based transport assays for WT and mutants of hOAT1. Error bars show the SEM. ns, $P > 0.05$; * $P \leq 0.05$; ** $P \leq 0.01$; and *** $P \leq 0.001$. (D) Competition binding of glibenclamide against 6-CF with WT and mutants. Data are means \pm SEM. (E) Comparison of glibenclamide binding (red) with cidofovir binding (gray) in the central site.

IC_{50} of this mutant for glibenclamide was increased compared to wild type (Y230F, $6.3 \pm 1.5 \mu\text{M}$; $P < 0.05$) (Fig. 4, C and D), highlighting its involvement in glibenclamide interactions.

Previous studies showed a range of chemically and structurally diverse small molecules that bind to the hOAT1, foreshadowing the plasticity of the site. In accordance with the promiscuity

suggested by these studies (35, 38), we found that glibenclamide binds to the same binding pocket as cidofovir, as well as other small molecules, but it protrudes more deeply into the “cradle” defined by TM1, TM4, and TM11, and forms extensive interactions with hOAT1 (Fig. 4E). This probably explains why glibenclamide exhibits ~60-fold higher binding affinity than cidofovir. Together, our data

reveal that the large central binding site is probably the basis of hOAT1 accommodating drugs of varying sizes.

The conserved aromatic residues for ligand binding

Secondary active membrane transport proteins typically use an alternating access model to translocate small molecules or ions across membranes. This model allows the substrate binding site to be exposed to alternate sides of the membrane without fully opening a channel between them (52, 53). Although all MFS proteins share a common structural fold, the unique characteristics of specific families may contribute to their distinct biological functions. To further investigate the conformational changes between the inward- and outward-facing states of hOAT1, we generated an outward-facing model of hOAT1 based on the structures of the outward-facing OCTs, hOCT1, and hOCT3. This model shows a high degree of structural similarity to hOCT1 and hOCT3, with C α root mean square deviation (RMSD) values of 0.110 and 1.266 Å, respectively (fig. S10E). In comparison to the inward-facing state of hOAT1, the NTD exhibits relative rigidity, while notable changes occur primarily in the CTD, resulting in an RMSD of 3.756 Å for C α atoms. On the extracellular side, structural rearrangements from the outward- to inward-facing state occur in the extracellular segments of TM7, TM9, TM10, TM11, and TM12, which move toward the central binding pocket, effectively closing the pathway to the extracellular solution. Conversely, in the intracellular portion, TM7, TM8, TM9, TM10, and TM11 shift away from the cavity, creating a fully open channel that connects the central cavity to the cytoplasm, while the intracellular portions of TM12 exhibit minimal displacement (Fig. 5, A to C).

Within the binding site, an aromatic bundle of residues has been implicated in ligand transport by hOCT1 and hOCT3 (36, 37, 54). Tyr³⁶¹ from hOCT1 and Tyr³⁶⁵ from hOCT3 have been identified as crucial components in substrate transport. The equivalent residue in hOAT1, Tyr³⁵³, acts as a gate on the extracellular side (Fig. 5D). In the outward-facing model of hOAT1, Tyr³⁵³ moves away from the NTD and CTD, thereby opening the extracellular permeation pathway (Fig. 5D). Meanwhile, Phe⁴⁴² from the intracellular side shifts closer to the NTD-CTD interface, effectively closing the pocket. The equivalent intracellular gate is formed by Tyr⁴⁵⁴ in hOCT3 and Trp³⁵⁴ in hOCT1 (Fig. 5D).

In hOAT1, both Tyr³⁵³ and Phe⁴⁴² play pivotal roles in substrate pocket closure, acting as gates on the extracellular and intracellular sides respectively. Mutation of Tyr³⁵³ to Ala in hOAT1 resulted in loss of transport activity, indicating the importance of Tyr³⁵³ in gating. In addition, Phe⁴⁴² can be replaced by nonaromatic residues such as Ala (Fig. 5E). It is worth noting that there is no such gate residue on the intracellular side of hOCT1. Tyr²²¹ of hOCT1 has been hypothesized to act as the bottom gate but the structural study does not support this assumption.

Tyr²³⁰ is involved in ligand binding both in rOAT1 and hOAT1 (36, 38), indicating its important role in ligand interaction within the central binding site. Alanine mutant of Tyr²³⁰ shows no activity (Fig. 5E). Trp³⁴⁶ and Phe⁴³⁸ are also conserved in OATs and OCTs (36, 37, 54). The residues Phe⁴³⁸ and Tyr²³⁰ are arranged in a face-to-face orientation in both outward- and inward-facing structure, forming a “π-sandwich” that serves to stabilize the ligand positioned between them. The similar π-sandwich pair observed in hOCT3 is Phe²⁵⁰ and Phe⁴⁵⁰ (37). Mutations of Phe³⁴⁶ and Phe⁴³⁸ to alanine resulted in a decrease in transport activity, providing further evidence for the essential role of these residues in protein function (Fig. 5E).

The conserved aromatic residues in the binding pocket of the SLC22 transporters probably suggest the importance of the aromatic interaction network in facilitating ligand binding across inward- and outward-facing conformations, which can partially explain the overlap in ligand selectivity between different SLC22 transporters (Fig. 5F). For example, OATs have been shown to have the ability to interact with cationic drugs (55), and both OATs and OCTs are known to interact in vitro and in vivo with zwitterionic or mildly “cationic” metabolites such as creatinine and polyamines (56–58).

DISCUSSION

The SLC22 family is composed of more than 30 transporters, which are responsible for the transport of organic cations (OCTs), anions (OATs), and zwitterions (59). Collectively, these transporters play a crucial role in determining the pharmacokinetics of a wide range of drugs and xenobiotics (9, 15). OAT1 (SLC22A6) is localized to the basolateral surface of the proximal tubule in kidney (2, 4) and plays an important role in drug excretion and potential DDIs (39–42). Inhibition of OAT1 is therapeutically used to alter drug efficacy and reduce toxicity. Therefore, developing more specific inhibitors for OAT1 could enable more precise interventions and clinical choices, enhancing drug concentration in the bloodstream while decreasing toxicity. A comprehensive understanding of transporter assembly and function will provide valuable insights for medical interventions and transporter organization. In this study, we describe the cryo-EM structures of hOAT1 and its complex with two drugs, providing direct insights into the organization of hOAT1 and its interactions with these drugs (figs. S3 to S4 and S6 to S8 and Figs. 3 and 4). Our findings indicate that hOAT1, purified in the presence of a mild ionic detergent DDM/CHS, is best described as a monomer. Both drugs for which we report cryo-EM structures, cidofovir and glibenclamide, are accommodated within the large central binding site, exhibiting partial overlap (Figs. 3 and 4). The expansive central binding site of hOAT1 facilitates the binding of a diverse range of small molecules, highlighting the poly-specificity of the transporter. This central pocket is composed of a bundle of conserved aromatic and hydrophobic residues that are crucial for ligand recognition. Mutations in these residues can substantially alter the transport activity of the transporter and its binding affinity for ligands (Fig. 5E). Variations in interactions within the central site may explain the differing binding affinities for distinct ligands.

Prior structural studies of hOCT1 and hOCT3 in different conformations have provided a structural framework for understanding the alternating access mechanism (29, 30, 45). During these conformational transitions, the NTD of hOCTs remains relatively static, while the CTD undergoes large scale movements to facilitate alternating access to the central pocket (36, 37, 54). To fully understand the transport mechanism of hOAT1, we generate outward-facing model of hOAT1 and compare it with the inward-facing state. Following a similar mechanism, the movement of the CTD domain of hOAT1 is expected to accompany opening or closing the central pocket to the solution during the transport cycle. Residues involved in ligand binding have been identified, and these residues are highly conserved within the SLC22 family. Mutations in these residues significantly affect the transport activity of hOAT1 and its binding affinity for ligands (Fig. 5). A deeper understanding of the structure of hOAT1 in its outward-facing conformation will be valuable for elucidating the transport mechanism.

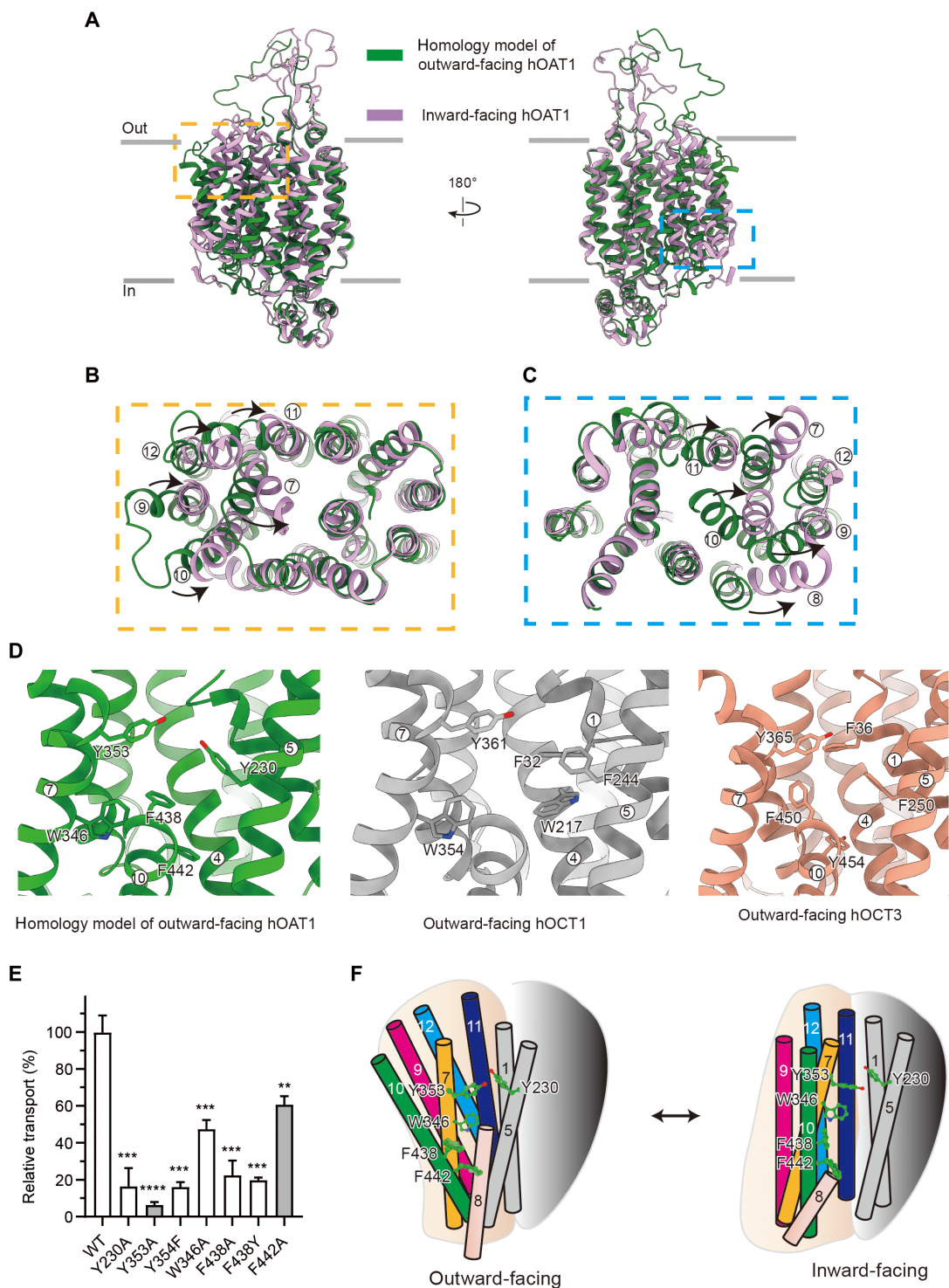


Fig. 5. Homology model of hOAT1 in the outward-facing conformation and cartoon of the aromatic cage in hOAT1. (A) The homology model of outward-facing hOAT1 superimposed with the structure of hOAT1 in the inward-facing conformation. (B) Top view of the comparison in (A). (C) Bottom view of the comparison in (A). (D) Comparison of the homology model of outward-facing hOAT1 and the structure of outward-facing hOCT1 and hOCT3, showing similar aromatic interaction network comprising conserved residues (Tyr^{230} , Trp^{346} , Tyr^{353} , Phe^{438} , and Phe^{442} in hOAT1; Phe^{32} , Trp^{217} , Phe^{244} , Trp^{354} , and Tyr^{361} in hOCT1; Phe^{36} , Phe^{250} , Tyr^{365} , Phe^{450} , and Tyr^{454} in hOCT3). (E) Cell-based transport assays for WT and mutants of hOAT1. Error bars show the SEM. ns, $P > 0.05$; * $P \leq 0.05$; ** $P \leq 0.01$; *** $P \leq 0.001$; and **** $P \leq 0.0001$. The uptake of 6-CF to Y353A and F442A from Fig. 4C is shown for comparison. (F) Schematic of the conserved aromatic cage in the substrate pocket of hOAT1.

In summary, the structures presented here offer a detailed glimpse into the organization of hOAT1 and the intricate structural interactions with two clinically relevant drugs of different sizes. The presence of a binding pocket of hOAT1 reveals how the transporter accommodates different size of drugs and which residues involve in the interactions. The insights obtained may offer opportunities for future drug design initiatives and the prediction of DDIs, thereby facilitating the reassessment and optimization of recommended drug dosages. Given the broad spectrum of drugs transported by OATs, our findings will contribute to a rationalization of drug disposition, particularly with regard to the diverse kinetics of drug uptake into the body.

METHODS

Protein expression and purification

The DNA encoding full-length hOAT1 (SLC22A6, uniprotKB Q4U2R8) was cloned into a modified C-terminally mCherry-tagged BacMam expression vector for baculovirus-based protein expression in mammalian cells, which also contains a C-terminal TEV cleavage site (ENLYFQG), followed by mCherry and streptavidin affinity tag (WSHPQFEK) and 10x His tag. Protein purification was similar with reported (60). Cells expressing hOAT1 were solubilized in ice-cold tris-buffered saline [20 mM tris (pH 8.0) and 150 mM NaCl], 5 mM CaCl₂, protease inhibitors [0.8 μM aprotinin, leupeptin (2 μg ml⁻¹), and 2 μM pepstatin], 1 mM phenylmethylsulfonyl fluoride, 20 mM DDM, and 2.5 mM CHS for 1 hour at 4°C. Unsolubilized materials were removed by centrifugation at 10,000g for 15 min. The supernatant was collected and applied for further centrifugation at 35,000 rpm for 40 min at 4°C (45 Ti fixed-angle rotor, Beckman). The supernatant was applied to pre-equilibrated streptavidin-linked resin by gravity flow. The protein-bound resin was washed with 10 column volumes of wash buffer [20 mM tris (pH 8.0), 150 mM NaCl, 5 mM CaCl₂, 1 mM DDM, and 0.2 mM CHS], and protein was eluted with an elution buffer [50 mM D-biotin, 20 mM tris (pH 8.0), 150 mM NaCl, 5 mM CaCl₂, 1 mM DDM, and 0.2 mM CHS]. The C-terminal mCherry tag of eluted protein was removed by TEV protease cleavage (1:50, w/w) overnight at 4°C. The digest reaction was loaded onto pre-equilibrated Ni-nitrilotriacetic acid beads by gravity flow to remove mCherry tag and uncleaved protein. The protein was further concentrated by a 50-kDa cutoff concentrator (Millipore) and subjected to SEC (Superdex 200 increase 10/300 column, GE Healthcare) running in SEC buffer [20 mM tris (pH 8.0), 150 mM NaCl, 5 mM CaCl₂, 1 mM DDM, and 0.2 mM CHS]. The peak fractions corresponding to hOAT1 were pooled, concentrated to 20 mg ml⁻¹, and used for cryo-EM sample preparation.

Cryo-EM sample preparation and data acquisition

The hOAT1 (3 μl) were applied to glow-discharged (60 s) Quantifoil grids (Au, 1.2/1.3 μm size/hole space, and 300 mesh). The grids were blotted for 2 s at 100% humidity at 4°C, followed by plunging into liquid ethane cooled by liquid nitrogen, using a Vitrobot Mark IV (Thermo Fisher Scientific).

Cryo-EM data were collected on a Titan Krios microscope (Thermo Fisher Scientific) equipped with a Quantum GIF energy filter with an energy slit of 20 eV (Gatan), operating at 300 kV. A Gatan K2 Summit direct electron detector was used to record movies in counting mode on the Krios at a nominal magnification of 165,000× with a pixel size of 0.85 Å. The defocus values ranged from

-1.7 to -1.2 μm. Each stack was exposed for 6 s and dose fractionated into 30 frames, with a total dose of 57.9 e⁻ Å⁻². Movie stacks were collected automatically using EPU software.

Cryo-EM image processing

The image processing of apo-hOAT1 was shown in fig. S3. In short, data processing was primarily carried out with RELION version 3.1 (61). Dose-fractionated images (5392) were motion corrected with MotionCor2 (62) followed by CTF estimation using CTFFIND4 (63). Micrographs (4980) were subjected to EMAN2.31 for neural network particle picking (64), which resulted in 3,520,140 particles. Rounds of reference-free 2D classifications and 3D classifications were performed in Relion3.1. Particles (389,365) were subjected to cryoSPARC (65) heterogeneous refinement with six classes and clear secondary structure in the TM region was observed in one class. Particles (107,629) were selected for homogeneous refinement, nonuniform refinement, and local refinement in cryoSPARC. The EM density map was sharpened using a negative B factor that was automatically determined in cryoSPARC using a Guinier plot. The resolution of the reconstructions was assessed using the Fourier shell correlation (FSC) criterion and a threshold of 0.143 in cryoSPARC. Local resolution of the final map was estimated in cryoSPARC.

The image processing of hOAT1 with cidofovir was shown in fig. S6. Dose-fractionated images (4002) were motion corrected with MotionCor2, followed by CTF estimation using CTFFIND4. Micrographs (3852) were subjected to EMAN2.31 for neural network particle picking, which resulted in 2,775,434 particles. Rounds of reference-free 2D classifications were performed in cryoSPARC version 4.4. Particles (2,492,626) were subjected to cryoSPARC heterogeneous refinement with six classes and clear secondary structure in the TM region was observed in one class. Particles (339,541) were selected for heterogeneous refinement in cryoSPARC and better-defined secondary structures in the TM region were observed in one class. Subsequently, 193,231 particles were selected for reference-based motion correction and further heterogeneous refinement, with one class showing further improvement of secondary structure in the TM region. Last, 129,163 particles were used for homogeneous refinement, nonuniform refinement, and local refinement in cryoSPARC. The EM density map was sharpened using a negative B factor that was automatically determined in cryoSPARC using a Guinier plot. The resolution of the reconstructions was assessed using the FSC criterion and a threshold of 0.143 in cryoSPARC. Local resolution of the final map was estimated in cryoSPARC.

The image processing of hOAT1 with glibenclamide was shown in fig. S6. Dose-fractionated images (8143) were motion corrected with MotionCor2, followed by CTF estimation using CTFFIND4. Micrographs (6567) were subjected to EMAN2.31 for neural network particle picking, which results in 4,363,859 particles. Rounds of reference-free 2D classifications were performed in cryoSPARC version 4.4. Particles (3,184,020) were subjected to heterogeneous refinement with six classes and clear secondary structure in the TM region was observed in two classes. Particles (1,399,003) were selected for heterogeneous refinement with six classes. After three rounds, clear secondary structure in the TM region was observed in one class. Particles (152,395) were selected for homogeneous refinement and nonuniform refinement in cryoSPARC. The EM density map was sharpened using a negative B factor that was automatically determined in cryoSPARC using a Guinier plot. The resolution of the reconstructions was assessed using the FSC criterion and a

threshold of 0.143 in cryoSPARC. Local resolution of the final map was estimated in cryoSPARC.

Model building and refinement

The AlphaFold2-predicted model served as an initial reference. The model was docked into the electron density using UCSF Chimera. Then, each individual residue was manually examined and adjusted to fit the map in Coot. Subsequently, the model was refined against the corresponding map in PHENIX. MolProbity was used to evaluate the stereochemistry and geometry of the structure. Cidofovir and glibenclamide were modeled into the cryo-EM map. Figures were prepared in UCSF Chimera and UCSF ChimeraX (66).

MD simulations

Molecular docking was performed using AutoDock Tools (67) and AutoDock Vina (68). To ensure the accuracy of docking simulations, the small molecules cvf and glb were preprocessed using AutoDock Tools. Preprocessing steps included optimizing molecular geometry and adjusting charge distribution, and the processed molecules were saved in PDBQT format. The protein model was also preprocessed using AutoDock Tools, including deletion of extraneous molecules and water molecules, as well as adding polar hydrogens. The processed protein structure was also saved in PDBQT format. Docking simulations of the preprocessed small molecules into the boxed region (20, 20, and 20 Å) of the protein were conducted using AutoDock Vina.

Subsequently, small molecules in the best-scored conformations were subjected to MD simulations in Desmond program. The Protein Preparation Wizard was used to remove water molecules, to complete missing side chains and loop regions, and to perform energy minimization. The OPLS2005 force field was applied to parameterize both the protein and small molecules, while the TIP3P water model was used for solvation. The protein-small molecule complex was embedded in a cubic water box, solvated, and neutralized by adding 0.150 M chloride and sodium ions. Initially, the system's energy was minimized for 50,000 steps using the steepest descent method. Subsequently, NVT and NPT equilibration simulations were performed for 50,000 steps each, with positional restraints applied to heavy atoms. During these equilibrations, the system temperature was maintained at 300 K, and the pressure was kept at 1 bar. After equilibration, a production MD simulation of 200 ns was carried out by applying a 0.1 N external force to the protein backbone atoms while leaving the ligand atoms unconstrained. Energy and coordinate trajectories were saved every 20 ps. Interaction patterns and dynamic trajectory animations were analyzed and visualized using Desmond (69) and ChimeraX.

Cell-based 6-CF transport assays

HEK293 cells were maintained in Dulbecco's minimum essential medium (Gibco, C11995500BT) supplemented with 10% fetal bovine serum under 5% CO₂ at 37°C. Cells per well were seeded into six-well plates and 24 hours later transfected using PEI [polyethyleneimine (YEASEN) 40816ES02] transfection reagent (2-μg DNA per 6 μg of PEI per well) with hOAT1 constructs containing a C-terminal mCherry tag in the vector pEG-Backman for 24 hours. Then, 0.5 × 10⁵ cells per well were seeded into 96-well plates for 24 hours.

For the assay, cells were washed three times with 100 μl of uptake buffer [composed of 135 mM NaCl, 5 mM KCl, 2.5 mM CaCl₂,

1.2 mM MgCl₂, 0.8 mM MgSO₄, 28 mM glucose, and 13 mM Hepes at (pH 7.2)] and then incubated with 100 μl of uptake buffer for 10 min. Subsequently, the cells were exposed to 100 μl of uptake buffer containing varying concentrations (0.03, 0.1, 0.3, 1, 3, 10, 30, and 100 μM) of 6-CF for 5 min. Following this, the cells were washed three times with 100 μl of ice-cold phosphate-buffered saline. The cells were then lysed by adding 100 μl of lysis buffer containing 20 mM tris at (pH 7.0) and 0.2% Triton X-100 for 5 min. The fluorescence intensity was measured using a microplate reader at an excitation/emission wavelength of 490/520 nm. Background fluorescence from cells without transfection was subtracted, and the data were normalized to 100%. The uptake data were subsequently fitted to the Michaelis-Menten equation $v = \frac{V_{max} \cdot S}{K_m + S}$. The maximum transport rate (V_{max}) and the Michaelis constant (K_m) were estimated by fitting the experimental profiles of uptake rate (v) versus substrate concentration (S) to this equation, using a nonlinear least-squares regression analysis implemented in GraphPad Prism software (GraphPad Software Inc., USA).

For the normalization of mutant transport activity, cells were lysed with 250 μl of RIPA lysis buffer [50 mM tris (pH 7.4), 150 mM NaCl, 1 mM EDTA-2Na, 1% Triton X-100, 1% sodium deoxycholate, and 0.1% SDS] at 4°C for 10 min, and the lysates were transferred to 96-well plates. The total protein concentration was determined using a BCA protein assay kit (Globio), and the optical density value was measured at 560 nm with a microplate reader. The transport activity was normalized on the basis of the relative protein concentrations.

To investigate the impact of ligands or inhibitors, the compound was introduced into the uptake buffer at the specified concentration. To determine the IC₅₀ values for the compounds, the uptake buffer containing 10 μM 6-CF was combined with varying concentrations of the compounds and incubated with the cells for 5 min. Each concentration was replicated three times to calculate SEs, and the entire experiment was conducted three times to determine the mean IC₅₀ value and SE. The data were analyzed using nonlinear regression to fit the equation $V = \frac{V_0}{[1 + (\frac{I}{IC_{50}})]}$, where V and V_0 represent the 6-CF uptake rates in the presence and absence of the inhibitor, respectively, and I is the inhibitor concentration, with n denoting the slope. The IC₅₀ value was subsequently converted to K_i using the equation $K_i = \frac{IC_{50}}{[1 + (\frac{C}{K_m})]}$, where C is the substrate concentration and K_m is the Michaelis constant.

Supplementary Materials

This PDF file includes:

Figs. S1 to S10

Table S1

REFERENCE AND NOTES

- G. D. Simonson, A. C. Vincent, K. J. Roberg, Y. Huang, V. Iwanij, Molecular cloning and characterization of a novel liver-specific transport protein. *J. Cell Sci.* **107** (4), 1065–1072 (1994).
- C. E. Lopez-Nieto, G. You, K. T. Bush, E. J. G. Barros, D. R. Beier, S. K. Nigam, Molecular cloning and characterization of NKT, a gene product related to the organic cation transporter family that is almost exclusively expressed in the kidney. *J. Biol. Chem.* **272**, 6471–6478 (1997).
- K. Mori, Y. Ogawa, K. Ebihara, T. Aoki, N. Tamura, A. Sugawara, T. Kuwahara, S. Ozaki, M. Mukoyama, K. Tashiro, I. Tanaka, K. Nakao, Kidney-specific expression of a novel mouse organic cation transporter-like protein. *FEBS Lett.* **417**, 371–374 (1997).
- M. Nishimura, S. Naito, Tissue-specific mRNA expression profiles of ATP-binding cassette and solute carrier transporter superfamilies. *Drug Metab. Pharmacokinet.* **20**, 452–477 (2005).

5. C. Hilgendorf, G. Ahlin, A. Seithel, P. Artursson, A.-L. Ungell, J. Karlsson, Expression of thirty-six drug transporter genes in human intestine, liver, kidney, and organotypic cell lines. *Drug Metab. Dispos.* **35**, 1333–1340 (2007).
6. H. Koepsell, The SLC22 family with transporters of organic cations, anions and zwitterions. *Mol. Aspects Med.* **34**, 413–435 (2013).
7. A. N. Rizwan, G. Burckhardt, Organic anion transporters of the SLC22 family: Biopharmaceutical, physiological, and pathological roles. *Pharm. Res.* **24**, 450–470 (2007).
8. S. K. Nigam, K. T. Bush, G. Martovetsky, S.-Y. Ahn, H. C. Liu, E. Richard, V. Bhatnagar, W. Wu, The organic anion transporter (OAT) family: A systems biology perspective. *Physiol. Rev.* **95**, 83–123 (2015).
9. S. K. Nigam, The SLC22 transporter family: A paradigm for the impact of drug transporters on metabolic pathways, signaling, and disease. *Annu. Rev. Pharmacol. Toxicol.* **58**, 663–687 (2018).
10. Y. Hagos, N. A. Wolff, Assessment of the role of renal organic anion transporters in drug-induced nephrotoxicity. *Toxins* **2**, 2055–2082 (2010).
11. M. Sakiyama, H. Matsuo, S. Shimizu, H. Nakashima, A. Nakayama, T. Chiba, M. Naito, T. Takada, H. Suzuki, N. Hamajima, K. Ichida, T. Shimizu, N. Shinomiya, A common variant of organic anion transporter 4 (OAT4/SLC22A11) gene is associated with renal underexcretion type gout. *Drug Metab. Pharmacokinet.* **29**, 208–210 (2014).
12. C.-Y. Sun, M.-S. Wu, C.-C. Lee, S.-H. Chen, K.-C. Lo, Y.-H. Chen, A novel SNP in the 5' regulatory region of organic anion transporter 1 is associated with chronic kidney disease. *Sci. Rep.* **8**, 8085 (2018).
13. M. A. Rizzo, S. Sallustio, V. Sueiro, V. Bertoni, H. Gonzalez-Torres, C. G. Musso, The importance of tubular function in chronic kidney disease. *Int. J. Nephrol. Renovasc. Dis.* **12**, 257–262 (2019).
14. S. M. Mihaile, J. Faria, M. F. J. Steffens, D. Stamatialis, M. C. Verhaar, K. G. F. Gerritsen, R. Masereeuw, Drugs commonly applied to kidney patients may compromise renal tubular uremic toxins excretion. *Toxins* **12**, 391 (2020).
15. S. W. Yee, K. M. Giacomini, Emerging roles of the human solute carrier 22 family. *Drug Metab. Dispos.* **50**, 1193–1210 (2021).
16. S. Masuda, H. Saito, K.-I. Inui, Interactions of nonsteroidal anti-inflammatory drugs with rat renal organic anion transporter, OAT-K1. *J. Pharmacol. Exp. Ther.* **283**, 1039–1042 (1997).
17. T. Cihlar, D. C. Lin, J. B. Pritchard, M. D. Fuller, D. H. Sweet, The antiviral nucleotide analogs cidofovir and adefovir are novel substrates for human and rat renal organic anion transporter 1. *Mol. Pharmacol.* **56**, 570–580 (1999).
18. S. H. Cha, T. Sekine, H. Kusuvara, E. Yu, J. Y. Kim, D. K. Kim, Y. Sugiyama, Y. Kanai, H. Endou, Molecular cloning and characterization of multispecific organic anion transporter 4 expressed in the placenta. *J. Biol. Chem.* **275**, 4507–4512 (2000).
19. H. Kimura, M. Takeda, S. Narikawa, A. Enomoto, K. Ichida, H. Endou, Human organic anion transporters and human organic cation transporters mediate renal transport of prostaglandins. *J. Pharmacol. Exp. Ther.* **301**, 293–298 (2002).
20. M. Takeda, S. Khamdang, S. Narikawa, H. Kimura, M. Hosoyamada, S. H. Cha, T. Sekine, H. Endou, Characterization of methotrexate transport and its drug interactions with human organic anion transporters. *J. Pharmacol. Exp. Ther.* **302**, 666–671 (2002).
21. X. Xue, L.-K. Gong, K. Maeda, Y. Luan, X.-M. Qi, Y. Sugiyama, J. Ren, Critical role of organic anion transporters 1 and 3 in kidney accumulation and toxicity of aristolochic acid I. *Mol. Pharmaceutics* **8**, 2183–2192 (2011).
22. S. Floerl, A. Kuehne, Y. Hagos, Functional characterization and comparison of human and mouse organic anion transporter 1 as drugs and pesticides uptake carrier. *Eur. J. Pharm. Sci.* **175**, 106217 (2022).
23. W. R. Wikoff, M. A. Nagle, V. L. Kouznetsova, I. F. Tsigelny, S. K. Nigam, Untargeted metabolomics identifies enterobiomass metabolites and putative uremic toxins as substrates of organic anion transporter 1 (Oat1). *J. Proteome Res.* **10**, 2842–2851 (2011).
24. V. S. Ermakov, J. C. Granados, S. K. Nigam, Remote effects of kidney drug transporter OAT1 on gut microbiome composition and urate homeostasis. *JCI Insight* **8**, e172341 (2023).
25. M. Hosoyamada, T. Sekine, Y. Kanai, H. Endou, Molecular cloning and functional expression of a multispecific organic anion transporter from human kidney. *Am. J. Physiol.* **276**, F122–F128 (1999).
26. J. E. Race, S. M. Grassl, W. J. Williams, E. J. Holtzman, Molecular cloning and characterization of two novel human renal organic anion transporters (hOAT1 and hOAT3). *Biochem. Biophys. Res. Commun.* **255**, 508–514 (1999).
27. M. A. Nagle, W. Wu, S. A. Eraly, S. K. Nigam, Organic anion transport pathways in antiviral handling in choroid plexus in Oat1 (Slc22a6) and Oat3 (Slc22a8) deficient tissue. *Neurosci. Lett.* **534**, 133–138 (2013).
28. N. Bakhshi, V. M. Arlt, A. Bahn, G. Burckhardt, D. H. Phillips, H. Glatt, Molecular evidence for an involvement of organic anion transporters (OATs) in aristolochic acid nephropathy. *Toxicology* **264**, 74–79 (2009).
29. M. K. Cook, E. M. Hagen, S. R. Feldman, Cidofovir in the management of non-genital warts: A review. *J. Drugs Dermatol.* **22**, 1009–1016 (2023).
30. K. C. Cundy, B. G. Petty, J. Flaherty, P. E. Fisher, M. A. Polis, M. Wachsman, P. S. Lietman, J. P. Lalezari, M. J. Hitchcock, H. S. Jaffe, Clinical pharmacokinetics of cidofovir in human immunodeficiency virus-infected patients. *Antimicrob. Agents Chemother.* **39**, 1247–1252 (1995).
31. J. P. Lalezari, R. J. Stagg, B. D. Kuppermann, G. N. Holland, F. Kramer, D. V. Ives, M. Youle, M. R. Robinson, W. L. Drew, H. S. Jaffe, Intravenous cidofovir for peripheral cytomegalovirus retinitis in patients with AIDS. A randomized, controlled trial. *Ann. Intern. Med.* **126**, 257–263 (1997).
32. E. K. Berggren, K. A. Boggess, Oral agents for the management of gestational diabetes. *Clin. Obstet. Gynecol.* **56**, 827–836 (2013).
33. A. P. Babenko, L. Aguilar-Bryan, J. Bryan, A view of sur/K_{ir}6.X, K_{ATP} channels. *Annu. Rev. Physiol.* **60**, 667–687 (1998).
34. Y. Uwai, H. Saito, Y. Hashimoto, K.-I. Inui, Inhibitory effect of anti-diabetic agents on rat organic anion transporter rOAT1. *Eur. J. Pharmacol.* **398**, 193–197 (2000).
35. J. L. Parker, T. Kato, G. Kuteyi, O. Sitsel, S. Newstead, Molecular basis for selective uptake and elimination of organic anions in the kidney by OAT1. *Nat. Struct. Mol. Biol.* **30**, 1786–1793 (2023).
36. Y. C. Zeng, M. Sobti, A. Quinn, N. J. Smith, S. H. J. Brown, J. I. Vandenberg, R. M. Ryan, M. L. O'Mara, A. G. Stewart, Structural basis of promiscuous substrate transport by organic cation transporter 1. *Nat. Commun.* **14**, 6374 (2023).
37. B. Khanppavar, J. Maier, F. Herborg, R. Gradišek, E. Lazzarin, D. Luethi, J.-W. Yang, C. Qi, M. Holy, K. Jäntschi, O. Kudlacek, K. Schicker, T. Werge, U. Gether, T. Stockner, V. M. Korkhov, H. H. Sitte, Structural basis of organic cation transporter-3 inhibition. *Nat. Commun.* **13**, 6714 (2022).
38. T. Dou, T. Lian, S. Shu, Y. He, J. Jiang, The substrate and inhibitor binding mechanism of polyspecific transporter OAT1 revealed by high-resolution cryo-EM. *Nat. Struct. Mol. Biol.* **30**, 1794–1805 (2023).
39. B. M. Tune, Nephrotoxicity of beta-lactam antibiotics: Mechanisms and strategies for prevention. *Pediatr. Nephrol.* **11**, 768–772 (1997).
40. M. Li, G. D. Anderson, J. Wang, Drug-drug interactions involving membrane transporters in the human kidney. *Expert Opin. Drug Metab. Toxicol.* **2**, 505–532 (2006).
41. International Transporter Consortium, K. M. Giacomini, S.-M. Huang, D. J. Tweedie, L. Z. Benet, K. L. R. Brouwer, X. Chu, A. Dahlin, R. Evers, V. Fischer, K. M. Hillgren, K. A. Hoffmaster, T. Ishikawa, D. Keppler, R. B. Kim, C. A. Lee, M. Niemi, J. W. Polli, Y. Sugiyama, P. W. Swaan, J. A. Ware, S. H. Wright, S. W. Yee, M. J. Zamek-Gliszczynski, L. Zhang, Membrane transporters in drug development. *Nat. Rev. Drug Discov.* **9**, 215–236 (2010).
42. A. Emami Riedmaier, A. T. Nies, E. Schaeffeler, M. Schwab, Organic anion transporters and their implications in pharmacotherapy. *Pharmacol. Rev.* **64**, 421–449 (2012).
43. A. Ortiz, P. Justo, A. Sanz, R. Melero, C. Caramelo, M. F. Guerrero, F. Strutz, G. Müller, A. Barat, J. Egido, Tubular cell apoptosis and cidofovir-induced acute renal failure. *Antivir. Ther.* **10**, 185–190 (2005).
44. S. N. Liu, Z. Desta, B. T. Gufford, Probenecid-boosted tenofovir: A physiologically-based pharmacokinetic model-informed strategy for on-demand HIV preexposure prophylaxis. *CPT Pharmacometrics Syst. Pharmacol.* **9**, 40–47 (2020).
45. A. L. VanWert, D. H. Sweet, Impaired clearance of methotrexate in organic anion transporter 3 (Slc22a8) knockout mice: A gender specific impact of reduced folates. *Pharm. Res.* **25**, 453–462 (2008).
46. T. Kawasaki, Y. Takeichi, M. Tomita, Y. Uwai, F. Epifano, S. Fiorito, V. A. Taddeo, S. Genovese, T. Nabekura, Effects of phenylpropanoids on human organic anion transporters hOAT1 and hOAT3. *Biochem. Biophys. Res. Commun.* **489**, 375–380 (2017).
47. C. Martinelli, A. Farese, A. del Mistro, S. Giorgini, I. Ruffino, Resolution of recurrent perianal condylomata acuminata by topical cidofovir in patients with HIV infection. *J. Eur. Acad. Dermatol. Venereol.* **15**, 568–569 (2001).
48. E. S. Ho, D. C. Lin, D. B. Mendel, T. Cihlar, Cytotoxicity of antiviral nucleotides adefovir and cidofovir is induced by the expression of human renal organic anion transporter 1. *J. Am. Soc. Nephrol.* **11**, 383–393 (2000).
49. T. Keller, B. Egenberger, V. Gorboulev, F. Bernhard, Z. Uzelac, D. Gorbunov, C. Wirth, S. Koppatz, V. Dötsch, C. Hunte, H. H. Sitte, H. Koepsell, The large extracellular loop of organic cation transporter 1 influences substrate affinity and is pivotal for oligomerization. *J. Biol. Chem.* **286**, 37874–37886 (2011).
50. S. Brast, A. Grabner, S. Sucic, H. H. Sitte, E. Hermann, H. Pavenstädt, E. Schlatter, G. Ciarimboli, The cysteines of the extracellular loop are crucial for trafficking of human organic cation transporter 2 to the plasma membrane and are involved in oligomerization. *FASEB J.* **26**, 976–986 (2012).
51. J. L. Perry, N. Dembla-Rajpal, L. A. Hall, J. B. Pritchard, A three-dimensional model of human organic anion transporter 1: Aromatic amino acids required for substrate transport. *J. Biol. Chem.* **281**, 38071–38079 (2006).
52. D. C. Gadsby, Ion channels versus ion pumps: The principal difference, in principle. *Nat. Rev. Mol. Cell Biol.* **10**, 344–352 (2009).
53. Y. Shi, Common folds and transport mechanisms of secondary active transporters. *Annu. Rev. Biophys.* **42**, 51–72 (2013).

54. Y. Suo, N. J. Wright, H. Guterres, J. G. Fedor, K. J. Butay, M. J. Borgnia, W. Im, S.-Y. Lee, Molecular basis of polyspecific drug and xenobiotic recognition by OCT1 and OCT2. *Nat. Struct. Mol. Biol.* **30**, 1001–1011 (2023).
55. S.-Y. Ahn, S. A. Eraly, I. Tsigelny, S. K. Nigam, Interaction of organic cations with organic anion transporters. *J. Biol. Chem.* **284**, 31422–31430 (2009).
56. S. Y. Ahn, N. Jamshidi, M. L. Mo, W. Wu, S. A. Eraly, A. Dnyanmote, K. T. Bush, T. F. Gallegos, D. H. Sweet, B. Ø. Palsson, S. K. Nigam, Linkage of organic anion transporter-1 to metabolic pathways through integrated “omics”-driven network and functional analysis. *J. Biol. Chem.* **286**, 31522–31531 (2011).
57. Y. Imamura, N. Murayama, N. Okudaira, A. Kurihara, O. Okazaki, T. Izumi, K. Inoue, H. Yuasa, H. Kusuvara, Y. Sugiyama, Prediction of fluoroquinolone-induced elevation in serum creatinine levels: A case of drug-endogenous substance interaction involving the inhibition of renal secretion. *Clin. Pharmacol. Ther.* **89**, 81–88 (2011).
58. V. Vallon, S. A. Eraly, S. R. Rao, M. Gerasimova, M. Rose, M. Nagle, N. Anzai, T. Smith, K. Sharma, S. K. Nigam, T. Rieg, A role for the organic anion transporter OAT3 in renal creatinine secretion in mice. *Am. J. Physiol. Renal Physiol.* **302**, F1293–F1299 (2012).
59. H. Koepsell, Organic cation transporters in health and disease. *Pharmacol. Rev.* **72**, 253–319 (2020).
60. X. Wu, T. Shang, X. Lü, D. Luo, D. Yang, A monomeric structure of human TMEM63A protein. *Proteins* **92**, 750–756 (2024).
61. J. Zivanov, T. Nakane, B. O. Forsberg, D. Kimanius, W. J. H. Hagen, E. Lindahl, S. H. W. Scheres, New tools for automated high-resolution cryo-EM structure determination in RELION-3. *eLife* **7**, e42166 (2018).
62. S. Q. Zheng, E. Palovcak, J.-P. Armache, K. A. Verba, Y. Cheng, D. A. Agard, MotionCor2: Anisotropic correction of beam-induced motion for improved cryo-electron microscopy. *Nat. Methods* **14**, 331–332 (2017).
63. A. Rohou, N. Grigorieff, CTFFIND4: Fast and accurate defocus estimation from electron micrographs. *J. Struct. Biol.* **192**, 216–221 (2015).
64. M. Chen, W. Dai, S. Y. Sun, D. Jonasch, C. Y. He, M. F. Schmid, W. Chiu, S. J. Ludtke, Convolutional neural networks for automated annotation of cellular cryo-electron tomograms. *Nat. Methods* **14**, 983–985 (2017).
65. A. Punjani, J. L. Rubinstein, D. J. Fleet, M. A. Brubaker, cryoSPARC: Algorithms for rapid unsupervised cryo-EM structure determination. *Nat. Methods* **14**, 290–296 (2017).
66. E. F. Pettersen, T. D. Goddard, C. C. Huang, G. S. Couch, D. M. Greenblatt, E. C. Meng, T. E. Ferrin, UCSF Chimera—A visualization system for exploratory research and analysis. *J. Comput. Chem.* **25**, 1605–1612 (2004).
67. G. M. Morris, R. Huey, W. Lindstrom, M. F. Sanner, R. K. Belew, D. S. Goodsell, A. J. Olson, AutoDock4 and AutoDockTools4: Automated docking with selective receptor flexibility. *J. Comput. Chem.* **30**, 2785–2791 (2009).
68. O. Trott, A. J. Olson, AutoDock Vina: Improving the speed and accuracy of docking with a new scoring function, efficient optimization and multithreading. *J. Comput. Chem.* **31**, 455–461 (2010).
69. M. Bergdorf, A. Robinson-Mosher, X. Guo, K.-H. Law, D. E. Shaw, Desmond/GPU Performance as of April 2021 (2021); <https://deshawresearch.com/resources.html>.

Acknowledgments

Funding: Cryo-EM data were collected on Can Cong at SKLB West China Cryo-EM Center and processed at SKLB Duyu High Performance Computing Center in West China Hospital. This work was supported by the startup funding of West China hospital, Sichuan University, and Tianfu Emei plan of Sichuan province to D.Y., National Key Research and Development Program of China (2022YFC2303700), Natural Science Foundation of China (NSFC 32222040 and 32070049), and 1.3.5 Project for Disciplines Excellence of West China Hospital (ZYYC21006) to Z.S. **Author**

contributions: D.Y. designed the project. D.Y., Z.S., K.W., and B.K. supervised the project. X.W. and S.F. performed protein purification and the biochemical experiments. Y.L. and Z.S. performed cryo-EM screening, data collection, model building, and refinement. H.M. and B.K. performed the MD simulation. D.Y. wrote the manuscript with input from all authors. All authors contributed to editing and manuscript preparation. **Competing interests:** The authors declare that they have no competing interests. **Data and materials availability:** All data needed to evaluate the conclusions in this paper are present in the paper and/or the Supplementary Materials. The cryo-EM maps and associated atomic coordinate models have been deposited in the wwPDB OneDep System under PDB ID and EMDB accession codes of 9J02 and EMD-61046 for apo-hOAT1, 9J04 and EMD-61048 for hOAT1 with cidofovir, and 9J06 and EMD-61050 for hOAT1 with glibenclamide.

Submitted 18 August 2024

Accepted 15 January 2025

Published 14 February 2025

10.1126/sciadv.ads5405